SUPPORTING INFORMATION

for

Development of an Inline Tube-in-Tube Solvent Exchanger for Continuous-flow Swap from High- to Low-boiling Solvent

Jiale Wu [†,‡], Xianjing Zheng [†,‡], Li Wan [†,‡], Yuan Tao [†,‡],

Dang Cheng [†,‡,*], Fener Chen [†,‡,*]

[†] *Engineering Center for Catalysis and Synthesis of Chiral Molecules, Department of Chemistry, Fudan University, 220 Handan Road, Shanghai 200433, China*

[‡] *Shanghai Engineering & Technology Research Center for Industrial Asymmetric Catalysis of Chiral Drugs, 220 Handan Road, Shanghai 200433, China*

*Corresponding authors:

dcheng@fudan.edu.cn (D. Cheng);

rfchen@fudan.edu.cn (F. E. Chen)

Table of Contents

1 Numerical method

The three dimensional geometry of the tube-in-tube device is shown in Figure S1. The outer tube and inner tube were co-axially assembled with the gas inlet and outlet installed horizontally and oppositely. The length of the outer tube (L_{ot}) was 25~50 cm, its inner diameter ($D_{i,ot}$) ranged from 4.0~6.0 mm. The length of the inner tube (i.e., liquid inlet, L_{it}) was 4.0 cm, and its inner diameter ($D_{i,it}$) was 1.0 mm. The length of the gas inlet ($L_{g,in}$) was 3.0 mm, and its inner diameter ($D_{g,in}$) was 1.0 mm. The length of the gas outlet ($L_{g,out}$) was 3.0 mm, and its inner diameter ($D_{g,out}$) was 1.0 mm.

Due to its plane symmetry, only a half of the full geometry was employed in the simulations in order to reduce computational cost. The geometry is discretized using a combination of hexahedral and prism elements. Because the tube-in-tube device had a high aspect ratio, hence the geometry used in the computations was scaled by a factor of 20 in order to further reduce computational burden.

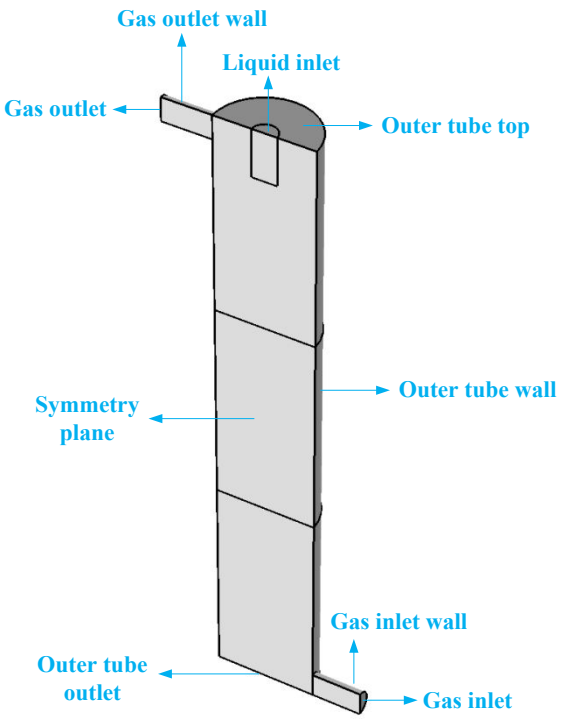

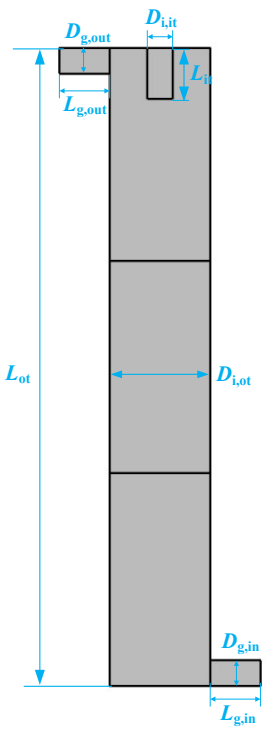

(a) 3D view (b) Dimensions of the device

Figure S1. Geometry of the tube-in-tube device.

The governing equations were implemented in the finite element approach based solver COMSOL Multiphysics. Talor-Hood elements were adopted in the spatial discretization. [1] Thus, piecewise-quadratic interpolation was performed for both the velocity $\mathbf{u}$ and order parameter φ, while piecewise-linear interpolation was applied for the pressure p, chemical potential G and temperature T. The initial time-step was 1.0×10^{-6} s. The implicit second-order backward differentiation formula (BDF) approach with an adaptive time-stepping was used in solving the governing equations. The direct solver PARDISO was employed to solve the discretized equation system. The boundary conditions applied are summarized in Table S1.

Table S1. Boundary conditions employed in the simulations.

Boundary name	Momentum equation	Phase field equation	Energy equation
Gas inlet	$\mathbf{u}=-U_0\mathbf{n}$	$\varphi=-1$	$T=T_0$
Gas inlet wall	$\mathbf{u}$=0	$\mathbf{n}\cdot\frac{\gamma\lambda}{\varepsilon^2}\nabla\Psi=0$ $\mathbf{n}\cdot\varepsilon^2\nabla\varphi=\varepsilon^2\cos(\theta_w)\lvert\nabla\varphi\rvert$ $\theta_w=\frac{\pi}{3}$ [rad]	$T=T_0$
Gas outlet	$\mathbf{K}=\mu\left(\nabla\mathbf{u}+(\nabla\mathbf{u})^T\right)$ $[-p\mathbf{I}+\mathbf{K}]=-p_0\mathbf{n}$	$-\nabla\cdot\mathbf{N}_\varphi$=0	$-\mathbf{n}\cdot(-k\nabla T)=0$
Gas outlet wall	$\mathbf{u}$=0	$\mathbf{n}\cdot\frac{\gamma\lambda}{\varepsilon^2}\nabla\Psi=0$ $\mathbf{n}\cdot\varepsilon^2\nabla\varphi=\varepsilon^2\cos(\theta_w)\lvert\nabla\varphi\rvert$ $\theta_w=\frac{\pi}{3}$ [rad]	$T=T_0$

Liquid inlet	$\mathbf{u} = -U_0\mathbf{n}$	$\varphi = 1$	$T = T_0$
Liquid inlet wall	$\mathbf{u}$=0	$\mathbf{n}\cdot\frac{\gamma\lambda}{\varepsilon^2}\nabla\Psi = 0$ $\mathbf{n}\cdot\varepsilon^2\nabla\varphi = \varepsilon^2\cos(\theta_w)\lvert\nabla\varphi\rvert$ $\theta_w = \frac{\pi}{3}$ [rad]	$Q = Q_0$
Liquid outlet	$\mathbf{K} = \mu\left(\nabla\mathbf{u} + (\nabla\mathbf{u})^T\right)$ $[-p\mathbf{I} + \mathbf{K}] = -p_0\mathbf{n}$	$-\nabla\cdot\mathbf{N}_\varphi$=0	$-\mathbf{n}\cdot(-k\nabla T) = 0$
Outer tube top	$\mathbf{u}$=0	$\mathbf{n}\cdot\frac{\gamma\lambda}{\varepsilon^2}\nabla\Psi = 0$ $\mathbf{n}\cdot\varepsilon^2\nabla\varphi = \varepsilon^2\cos(\theta_w)\lvert\nabla\varphi\rvert$ $\theta_w = \frac{\pi}{3}$ [rad]	$q_0 = h\cdot(T_{ext} - T)$
Outer tube wall	$\mathbf{u}$=0	$\mathbf{n}\cdot\frac{\gamma\lambda}{\varepsilon^2}\nabla\Psi = 0$ $\mathbf{n}\cdot\varepsilon^2\nabla\varphi = \varepsilon^2\cos(\theta_w)\lvert\nabla\varphi\rvert$ $\theta_w = \frac{\pi}{3}$ [rad]	$Q = Q_0$
Outer tube bottom	$\mathbf{K} = \mu\left(\nabla\mathbf{u} + (\nabla\mathbf{u})^T\right)$ $[-p\mathbf{I} + \mathbf{K}] = -p_0\mathbf{n}$	$-\nabla\cdot\mathbf{N}_\varphi$=0	$-\mathbf{n}\cdot(-k\nabla T) = 0$
Symmetry Plane	$\mathbf{K} = \mu\left(\nabla\mathbf{u} + (\nabla\mathbf{u})^T\right)$ $\mathbf{u}\cdot\mathbf{n} = 0$ $\mathbf{K}_n - (\mathbf{K}_n\cdot\mathbf{n})\mathbf{n} = 0$ $\mathbf{K}_n = \mathbf{K}\mathbf{n}$	$-\nabla\cdot\mathbf{N}_\varphi$=0	$-\mathbf{n}\cdot(-k\nabla T) = 0$

2 Grid convergence test

The mesh convergence test was performed before parametric study. The effect of the grid size on the numerical results was examined under the operating conditions of Q_L=0.5 ml/min, Q_G=80 ml/min and T=60 ℃. The geometrical parameters and relevant physical properties employed in the simulations are listed in Table S2.

Table S2. Input data used in the simulations.

Parameter	Value	Parameter	Value
L_{ot}	25 cm	ρ_L	958.4 kg/m^3
$D_{i,ot}$	4.0 mm	ρ_G	0.597 kg/m^3
$D_{i,it}$	1.0 mm	μ_L	277 μPa·S
L_{it}	4.0 cm	μ_G	12.55 μPa·S
$D_{g,in}$	1.0 mm	κ_L	679 mW/(m·K)
$D_{g,out}$	1.0 mm	κ_G	25 mW/(m·K)
$L_{g,in}$	3.0 mm	$C_{p,L}$	4.216 kJ/(kg·K)
$L_{g,out}$	3.0 mm	$C_{p,G}$	2.03 kJ/(kg·K)
h_{lg}	2257 kJ/kg	σ	59 mN/m
T_{sat}	100 ℃		

Five mesh models from coarse (A) to finest (E) were considered by controlling the maximum mesh size (MMS). The numerical results obtained from the five mesh models are shown in Figure S2. It can be seen that M_{ev} decreases with increasing mesh density from Mesh A to Mesh C. However, an inappreciable variation was observed in M_{ev} when the mesh density was further increased from Mesh C to Mesh E. Hence Mesh Model D was employed for further computations in this work.

Table S3. Mesh independence test.

Mesh Model	A	B	C	D	E
MMS	100 μm	70 μm	50 um	35 μm	30 μm
Mesh number	545909	683003	994971	1675235	2113311

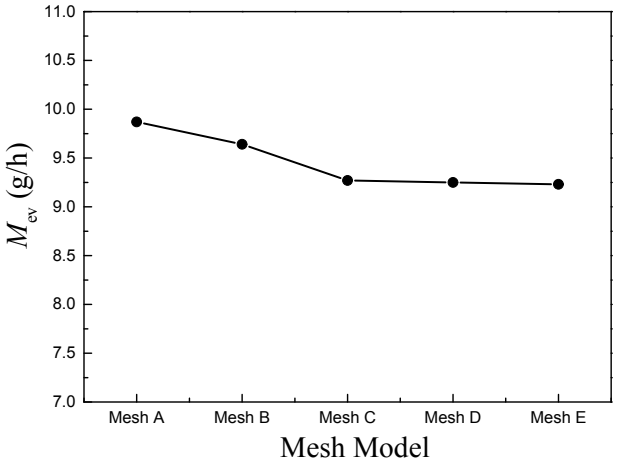

Figure S2. Effect of mesh density on the numerical results.

3 Model validation

In order to validate the numerical model, the simulation of a vapor bubble growing in a superheated liquid under zero gravity condition was carried out. The vapor bubble was initially spherical and at saturation temperature T_{sat}, which was located in a superheated liquid of temperature $T_{\infty} = T_{\mathrm{sat}} + 5$. The bubble grew due to the heat flux from the liquid to the vapor bubble surface. This problem has been widely used to validate phase-change CFD models [2-4]. Scriven [5] derived the analytical solution for the bubble radius (*r*) as

$$r = 2\beta\sqrt{\frac{\kappa_{\mathrm{L}}}{C_{\mathrm{p,L}}\rho_{\mathrm{L}}}t} \tag{2}$$

where κ_{L}, $C_{\mathrm{p,L}}$ and ρ_{L} are thermal conductivity, the specific heat capacity and the density of liquid, respectively, and β is the growth constant obtained from the following equation.

$$\frac{\rho_{\mathrm{L}}C_{\mathrm{p,L}}\left(T_{\infty}-T_{\mathrm{sat}}\right)}{\rho_{\mathrm{G}}\left(h_{\mathrm{lg}}+\left(C_{\mathrm{p,L}}-C_{\mathrm{p,G}}\right)\left(T_{\infty}-T_{\mathrm{sat}}\right)\right)} = 2\beta^{2}\int_{0}^{1}\left(\exp\left(-\beta^{2}\left(1-\varsigma\right)^{-2}-2\left(1-\frac{\rho_{\mathrm{G}}}{\rho_{\mathrm{L}}}\right)\varsigma-1\right)\right)d\varsigma \tag{3}$$

For the system of water and steam at 101.3 kPa, $\beta = 59$ was obtained.

To reduce computational cost, a 1/8 sector of the bubble was computed. As shown in Figure S3, the computational domain was a cube of size $0.4\ \mathrm{mm} \times 0.4\ \mathrm{mm} \times 0.4\ \mathrm{mm}$,

with the center of the spherical bubble, initially of radius 0.1 mm, located at one of its corners.

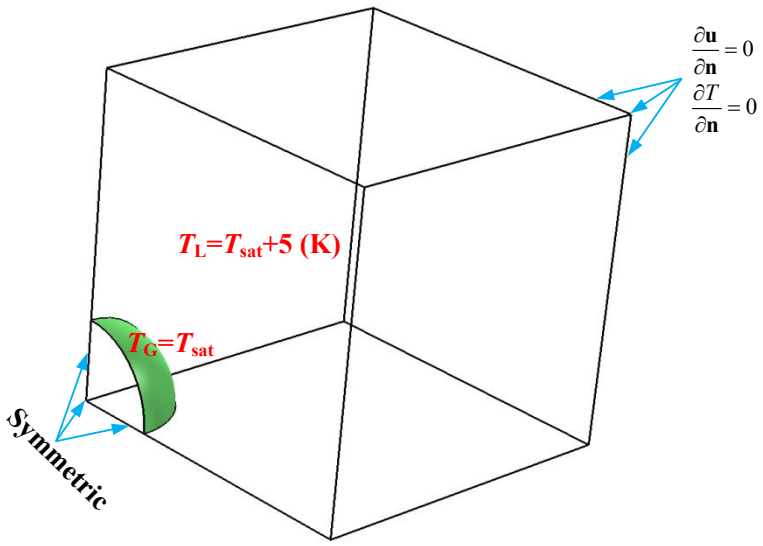

Figure S3. Schematic representation of the computational domain for the bubble growth problem.

The computed variation of the bubble radius with time is compared with the analytical solution in Figure S4. As can be seen, the numerical results are in very good agreement with the experimental ones, signifying that the numerical model was well-validated and it was employed for further computations in this study.

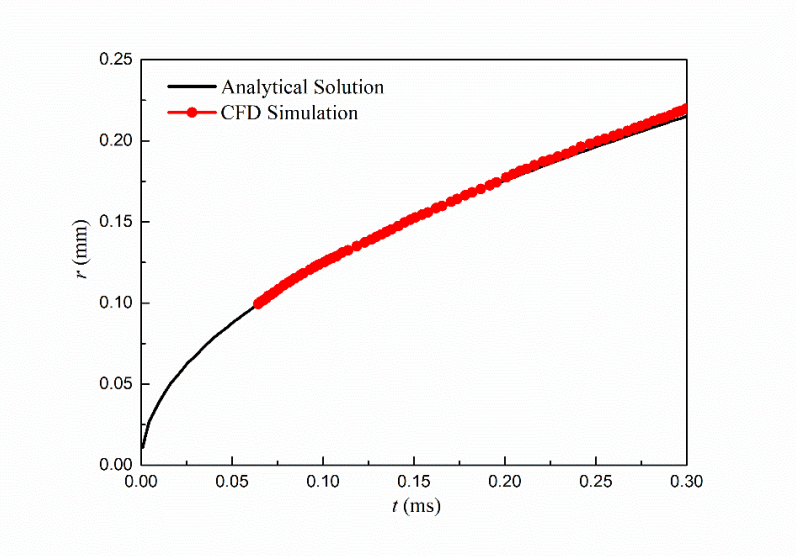

Figure S4. Comparison of bubble radius between simulations and analytical solution.

References

(1) Ern, A.; Guermond, J.-L. *Theory and Practice of Finite Elements*; Springer, Berlin, **2004.**

(2) Wang, Z.; Zheng, X.; Chryssostomidis, C.; Karniadakis, G. E. A phase-field method for boiling heat transfer. *J. Comput. Phys.* **2021**, 435, 110239.

(3) Sato, Y.; Ničeno, B. A sharp-interface phase change model for a mass-conservative interface tracking method. *J. Comput. Phys.* **2013**, 249, 127-161.

(4) Ferrari, A.; Magnini, M.; Thome, J.R. Numerical analysis of slug flow boiling in square microchannels. *Int. J. Heat Mass Transf.* **2018**, 123, 928-944.

(5) Scriven L.E. On the dynamics of phase growth. *Chem. Eng. Sci.* **1959**, 10, 1-13.